Evidence for tropospheric wind shear excitation of high phase-speed gravity waves reaching the mesosphere using ray tracing technique

M. Pramitha[1], M. Venkat Ratnam[1]*, Alok Taori[1], B. V. Krishna Murthy[2], D. Pallamraju[3], and S. Vijaya Bhaskar Rao[4]

[1]National Atmospheric Research Laboratory (NARL), Gadanki, India.

[2]B1, CEBROS, Chennai, India.

[3]Physical Research Laboratory (PRL), Ahmadabad, India

[4]Department of Physics, Sri Venketeswara University, Tirupati, India

* vratnam@narl.gov.in , Phone: +91-8585-272123, Fax: +91-8585-272018

Abstract

Reverse ray tracing method is successfully implemented in the Indian region for identification of the sources and propagation characteristics of high frequency gravity waves observed in the mesosphere using airglow emissions from Gadanki (13.5^{o}N, 79.2^{o}E) and Hyderabad (17.5^{o}N, 78.5^{o}E). Wave amplitudes are also traced back by including both radiative and diffusive damping. Background temperature and wind data obtained from MSISE-90 and HWM-07 models, respectively, are used for the ray tracing. For Gadanki region suitability of these models is tested. Further, a climatological model of background atmosphere for Gadanki region has been developed using a long-term of nearly 30 years of observations available from a variety of ground-based (MST radar, radiosonde, MF radar), rocket-, and satellite-borne measurements. For considering real-time atmospheric inputs, ERA-Interim products are utilized. By the reverse ray tracing method, the source locations for nine wave events could be identified to be in the upper troposphere, whereas, for five other events the waves got terminated in the mesosphere itself. Uncertainty in locating the terminal points in the horizontal direction is estimated to be within 50-100 km and 150-300 km for Gadanki and Hyderabad wave events, respectively. This uncertainty arises mainly due to non-consideration of the day-to-day variability in tidal amplitudes. As no convection in-and-around the terminal points are noticed, it is unlikely to be the source. Interestingly, large (~9 m/s/km) vertical shears in the horizontal wind are noted near the ray terminal points (at 10-12 km altitude) and are identified to be the source for generating the observed high phase speed, high frequency gravity waves. Conditions prevailing at the terminal points for each of the 14 events are also provided.

Key words: Gravity wave sources, reverse ray tracing, wave action, airglow, model outputs.

1. Introduction

Atmospheric gravity waves (GWs) play an important role in the middle atmospheric structure and dynamics. They transport energy and momentum from the source region (mainly troposphere) to the upper atmosphere. The waves are dissipated on encountering critical level, transferring energy and momentum to the mean flow and leading to changes in the thermal structure of the atmosphere (Fritts and Alexander 2003). Several sources are identified for the generation of GWs which include deep convection, orographic effect, vertical shear of horizontal wind and geostrophic adjustment. For GW generation from deep convection, basically three mechanisms are considered (Fritts and Alexander 2003). These are (i) pure thermal forcing (e.g. Salby and Garcia 1987; Alexander et al., 1995; Piani et al., 2000; Fritts and Alexander 2003; Fritts et al., 2006), (ii) mechanical oscillator effect (e.g. Clark et al., 1986; Fovell et al., 1992), (iii) obstacle effect (e.g. Clark et al., 1986; Pfister et al., 1993; Vincent and Alexander 2000). The importance of these depends upon the local shear vertical profile and time dependence of latent heat release. GWs from the convection source can have a wide range of phase speeds, frequencies and wavelengths unlike those from orography, which are generally confined to a particular frequency and phase speed (low) (e.g. Queney., 1948; Lilly and Kennedy 1973; Nastrom and Fritts 1992; Eckermann and Preusse 1999; Alexander et al., 2010). In the shear excitation mechanism two processes namely sub-harmonic interaction and envelope radiation (Fritts and Alexander 2003) exists. The latter process can yield horizontal scales of a few tens of kms and phase speeds comparable to the mean wind. The geostrophic adjustment source is effective mainly in high latitudes (e.g. O'Sullivan and Dunkerton 1995., Shin Suzuki et al., 2013; Plougonven and Zhang 2014).

In general, significant progress has been made in the understanding of the physical processes for generating the spectrum of GWs through both observations and modeling. However, identification of the exact sources for the generation of GWs and their parameterization in the models still remains a challenge (Geller et al., 2013). In order to identify the gravity wave sources, hodograph analysis has been widely used. Hodograph analysis can be used to identify the gravity wave parameters and which can be used as input parameters to the ray tracing. Using hodograph we can find whether the wave is propagating upward or downward and in this way indirectly we can locate the source at a particular altitude. However, this method is applicable only for medium and low frequency waves, as for the high frequency GWs the hodograph would not be an ellipse but nearly a straight line. Further, as it assumes monochromatic waves, it is not always applicable in the real atmosphere. Notwithstanding this limitation, using this method convection and vertical shear have been identified as the possible sources of the observed medium and low frequency GWs in the troposphere and lower stratosphere over many places (e.g., Venkat Ratnam et al., 2008). It becomes difficult to apply this method for GWs that are observed in the MLT region where simultaneous measurements of temperatures (with wind) would not be available.

A more appropriate method in such cases is ray tracing (Marks and Eckermann 1995), which is widely being used to identify the sources of GWs observed at mesospheric altitudes. Several studies (Hecht et al., 1994; Taylor et al., 1997; Nakamura et al., 2003; Gerrard et al., 2004; Brown et al., 2004; Wrasse et al., 2006; Vadas et al., 2009 and references therein) have been carried out to identify the sources for the GWs observed in the mesosphere using airglow images and in the stratosphere using radiosonde and lidar data (Guest et al., 2000; Hertzog et al., 2001). In mesospheric studies, important GW parameters, such as, periodicities and horizontal

wavelengths (and sometimes vertical wavelengths when two imagers are simultaneously used) are directly derived. A major limitation to the ray tracing method is the non-availability of realistic information of the background atmosphere, which is difficult to obtain with available suite of instrumentation and so identifying the source of the waves which propagate horizontally as well as vertically is difficult. Nevertheless, possible errors involved in identifying the terminal point of the waves with and without realistic background atmosphere have been estimated (e.g., Wrasse et al., 2006; Vadas et al., 2009).

Over the Indian region, several studies (Venkat Ratnam et al., 2008 and references therein) have been carried out for extracting GW parameters using various instruments (MST radar, Lidar and satellite observations). In a few studies (Kumar 2006., 2007; Dhaka et al., 2002; Venkat Ratnam et al., 2008; Debashis Nath et al., 2009; Dutta et al., 2009) possible sources in the troposphere for their generation are identified which include convection, wind shear, and topography.

In the present investigation, reverse ray tracing method is implemented to identify the sources of the GWs at mesospheric altitudes observed from an airglow imager located at Gadanki (13.5^{o}N, 79.2^{o}E) and from a balloon experiment which carried an ultraviolet imaging spectrograph from Hyderabad (17.5^{o}N, 78.5^{o}E). Using this we have traced the wave parameters and wave amplitudes along the ray path after including the radiative and turbulent damping and tried to find the sources for the observed waves. In Section 2 we described the instrumentation, in Section 3 the theory behind ray tracing, in Section 4 the background atmosphere used for ray tracing, in Section 5 application of the ray tracing method and in Section 6 identification of the sources for the observed waves.

2. Database

2.1. Airglow imager observations at Gadanki and methodology for extracting GW characteristics

The NARL Airglow Imager (NAI) located at Gadanki is equipped with 24 mm of Mamiya fish eye lens. It can monitor OH, O(^{1}S), and O(^{1}D) emissions and has a 1024x1024 pixels CCD as the detector and a field-of-view of NAI is 90^o avoiding non-linearity arising at higher zenith angles. In present study, only observations of O(^{1}S) emission which originate at ~93-100 km (with a peak emission altitude of ~97 km) are used. The exposure time used to measure the intensities of emissions was 70 s. After capturing the image it has been analyzed and corrected for the background brightness, star brightness and actual coordinates. The area covered in the image is 200 km x 200 km with a spatial resolution of 0.76 km near zenith and 0.79 km at the edges. More details of the NAI are discussed by Taori et al. (2013).

We have observed three wave events between 14:29-14:51 UTC, 15:44-15:50 UTC and 20:45-21:17 UTC on 17 March 2012 (Figure 1) and two wave events between 15:47 - 16:27 UTC and 16:31 - 16:54 UTC on 19 March 2012 in the O(^{1}S) airglow emission intensities. In these images crests of the waves are emphasized by yellow freehand lines and motion of the waves are apparent in the successive images shown one below the other. Red arrows indicate the direction of the propagation of the waves. Horizontal wavelengths of the GWs are determined by applying 2D FFT to the observed airglow images. The periods of the GWs are estimated by applying 1D FFT in time to the complex 2D FFT in space. Direction of propagation and phase speed of GWs are identified using successive images. More details of the methodology for estimating the GW parameters from NAI observations are provided in Taori et al. (2013). Table 1 summarizes the GW parameters extracted for the five wave events (G1 to G5) mentioned

above. In general, the waves corresponding to these events are moving north, north-west direction. Zonal (k) and meridional (l) wave numbers are calculated using the relations $k = k_h \cos\phi$ and $l = k_h \sin\phi$ where k_h is the horizontal wave number and ϕ is the horizontal direction of propagation observed from the airglow imager. The vertical wavelengths are calculated using the GW dispersion relation

$$\omega_{ir}^2 = \frac{N^2(k^2 + l^2) + f^2(m^2 + \alpha^2)}{k^2 + l^2 + m^2 + \alpha^2} \qquad (1)$$

where ω_{ir} is the intrinsic frequency of the wave, N is the Brunt- Väiäsälä frequency, f is the coriolis frequency and m is the vertical wave number. Zonal, meridional and vertical wavelengths can be derived from the parameters given in Table 1 Preusse et al.(2008) reported that around 60% of the waves which are launched around 20 km with horizontal wavelength greater than 20 km and high phase speed can reach MLT altitudes and we try to explore our findings related to this. The background atmosphere used for ray tracing is developed using 30 years of observations from various sources and will be discussed more in section 4.

2.2. Daytime GW observations at Hyderabad obtained through optical emissions

A multi-wavelength imaging echelle spectrograph (MISE) is used to obtain daytime emission intensities of oxygen emissions at 557.7 nm, 630.0 nm and 777.4 nm in the MLT region at Hyderabad. MISE obtains high resolution spectra of daytime skies which are compared with the reference solar spectrum. The difference obtained between the two yields information on the airglow emissions. The details of the emission extraction process and calibration procedures of the emission intensities and the salient results obtained in terms of wave coupling of atmospheric regions demonstrating the capability of this technique have been described elsewhere (Pallamraju et al., 2013; Laskar et al., 2013). In the present experiment, the slit oriented along the magnetic meridian enabled information on the meridional scale size of waves (λ_y) at O(^{1}S)

emission altitude of ~ 100 km (in the daytime). An ultraviolet imaging spectrograph (UVIS) with its slit oriented in the east-west direction was flown on a high-altitude balloon (on 8 March 2010) which provided information on the zonal scale sizes of waves (λ_x) using the OI 297.2 nm emissions that originate at ~ 120 km. Both MISE and UVIS are slit spectrographs with array detectors providing 2-D information with one direction yielding high spectral resolution spectrum (0.012 nm at 589.3 nm and 0.2 nm at 297.2 nm for MISE and UVIS, respectively), and the orthogonal direction yielding information on the dynamics over 330 km (in the y-direction for OI 557.7 nm emission) and 170 km (in the x-direction for the OI 297.2 nm emission). The spatial resolutions of these measurements are around 50 km and 11 km, respectively. The details of the experiment and the wave characteristics in terms of λ_x, λ_y, λ_H (horizontal scale sizes), time periods (τ), propagation speeds (c_H) and propagation direction (θ_H) obtained by this instrument at a representative altitude of 100 km are described in detail in Pallamraju et al. (2014). Nine events from this experiment occurred on 8 March 2010 are considered in the present study for investigating their source regions and are marked as H1 to H9 in Table 1. All the observed wave events at Gadanki and Hyderabad whose parameters are given in Table 1 correspond to high frequency high phase speed gravity waves as seen from their large vertical wavelengths, small periods and high phase speeds (Table 1).

2.3. Outgoing Long-wave Radiation (OLR) and Brightness Temperature in the Infrared band (IR BT)

Satellite data of OLR / IR BT are used as proxy for tropical deep convection. In general, the daily NOAA interpolated OLR can be used to obtain information on synoptic scale convection. However, for local convection on smaller spatial and temporal scales, the IR BT data merged from all available geostationary satellites (GOES-8/10, METEOSAT-7/5 GMS) are

obtained from Climate Prediction Center, National Centre for Environment Prediction (NCEP) (source: ffp://disc2.nascom.nasa.gov/data/s4pa/TRMM_ANCILLARY/MERG/). The merged IR BT with a pixel resolution of 4 km is available from 60^oN to 60^oS (geo-stationary). The data in the East-west begins from 0.082^o E with grid increment of 0.03637^o of longitude and that in the North-South from 59.982^o N with grid increment of 0.03638^o of latitude (Janowiak et al., 2001). The BT dataset is retrieved for every half an hour interval over regions of ±5° around Gadanki and Hyderabad on 17 March 2012 and 8 March 2010, respectively, to see whether any convective sources were present over these locations. Since the waves under study are high frequency waves propagating at high phase speeds with smaller horizontal wavelengths, a maximum of 5^oX5^o grid is considered to be adequate. In general, the regions with OLR < 240 W/m^2 are treated as convective areas.

3. Reverse ray tracing method

We followed basically the treatment of ray tracing given by Marks and Eckermann (1995). Note that the ray tracing theory is applicable only when WKB approximation is valid. When the WKB parameter δ given by

$$\delta = \frac{1}{m^2}\left|\frac{\partial m}{\partial z}\right| \approx \left|\frac{1}{C_{gz}m^2}\frac{dm}{dt}\right| \qquad (2)$$

where C_{gz} is the vertical group velocity, m is the vertical wave number, t is the time and z is the altitude, is less than unity, the approximation is taken to be valid.

In order to calculate the wave amplitude we used the wave action equation of the form

$$\frac{\partial A}{\partial t} + \nabla.(C_g A) = -\frac{2A}{\tau} \qquad (3)$$

where $A = E/\omega_{ir}$ represents the wave action density, C_g represents the group velocity vector and $E = \frac{\rho_0}{2}[\overline{u'^2} + \overline{v'^2} + \overline{w'^2} + N^2\overline{\zeta'^2}]$ represents the wave energy density being the sum of kinetic and potential energy components, as described by wave perturbations in zonal, meridional and vertical velocities (u', v', w'), and vertical displacement (ζ'). Here ρ_0 is the background density and τ is the damping time scale (Marks and Eckermann, 1995). Using the peak horizontal velocity amplitude along the horizontal wave vector we can calculate the wave action density using the equation:

$$A = \frac{1}{4}\frac{\rho_0 |\hat{u}_{\backslash\backslash}|^2}{\omega_{ir}}\{1 + \frac{f^2}{\omega_{ir}^2} + \frac{N^2 + \omega_{ir}^2}{N^2 - \omega_{ir}^2}(1 - \frac{f^2}{\omega_{ir}^2})\} \quad (4)$$

In order to avoid spatial integration in the wave action equation we can write Equation (3) in terms of the vertical flux of wave action $F = C_{gz}A$, where F is the vertical flux of wave action and C_{gz} is vertical component of the group velocity. Assuming negligible contribution from the higher order terms, the Equation (4) can be written as:

$$\frac{dF}{dt} = -\frac{2}{\tau}F \quad (5)$$

As the wave moves through the atmosphere, amplitude damping takes place which is mainly due to eddy diffusion and infrared radiative cooling by CO_2 and O_3. At higher altitudes (above about 100 km) molecular diffusion becomes important as compared to the eddy diffusion. We can calculate the damping rate due to diffusion using:

$$\tau_D^{-1} = D(k^2 + l^2 + m^2 + \alpha^2) \quad (6)$$

Where, $D = D_{Eddy} + D_{molecular}$, represents the sum of eddy and molecular diffusivities. In order to calculate the infrared radiative damping we used Zhu (1993) damping rate calculation method from 20-100 km. The total damping rate is calculated using the following equation:

$$\tau^{-1} = \frac{\tau_r^{-1}\left(\frac{1-f^2/\omega_{ir}^2}{1-\omega_{ir}^2/N^2}\right) + \tau_D^{-1}\left(1+\frac{f^2}{\omega_{ir}^2}+\frac{1-f^2/\omega_{ir}^2}{N^2/\omega_{ir}^2-1}+\mathrm{Pr}^{-1}\frac{1-f^2/\omega_{ir}^2}{1-\omega_{ir}^2/N^2}\right)}{\left\{1+\frac{f^2}{\omega_{ir}^2}+\frac{N^2+\omega_{ir}^2}{N^2-\omega_{ir}^2}\left(1-\frac{f^2}{\omega_{ir}^2}\right)\right\}} \quad (7)$$

Where Pr is prandtl number. Note that for high frequency waves diffusion damping effect will be less.

4. Background atmosphere

In order to carryout reverse ray-tracing, information on background atmospheric parameters (U, V and T) is required right from the initial point (mesosphere) to the termination point (usually the troposphere). In general, there is no single instrument which can probe the troposphere, stratosphere, and mesosphere simultaneously. Note that in order to trace the ray we require atmospheric parameters for a specified latitude-longitude grid. Since the observed wave events belong to high frequencies (GWs with short horizontal wavelengths), we require the background information at least for grid sizes of 5^o x 5^o around Gadanki and Hyderabad. For the information on temperature and density at the required grids, we used Extended Mass Spectrometer and Incoherent Scatter Empirical Model (MSISE-90) data (Hedin, 1991) from surface to 100 km with an altitude resolution of 0.1 km for 0.1^ox0.1^o grid around these locations. Note that the MSISE-90 model is an empirical model which provides temperature and density data from the surface to the thermosphere. For horizontal winds at required grids, we used the outputs from the Horizontal Wind Model (HWM-07) (Drob et al., 2008) data. This model has

238 been developed by using a total of 60 x 10^6 observations available from 35 different instruments
239 spanning 50 years. Further, long-term data available from a variety of instruments (MST radar,
240 MF radar, Rocketsonde, radiosonde, HRDI /UARS and SABER/TIMED satellites) in-and-
241 around ($\pm5^o$) Gadanki have been used to develop a background climatological model profiles of
242 U, V, and T on monthly basis. Details of the data used to develop the background temperature
243 and horizontal winds are provided in Table 2. Monthly mean contours of temperature, zonal and
244 meridional winds obtained from the climatological model (hereafter referred to as the Gadanki
245 model) are shown in Figure 2. In general, major features of the background atmospheric structure
246 for a typical tropical region can be noticed from this figure. Tropopause, stratopause, and
247 mesopause altitudes are located at around 16-18 km, 48-52 km, and 98-100 km with
248 temperatures 190-200 K, 260-270 K and 160-170 K, respectively. Mesospheric semi-annual
249 oscillation around 80-85 km is also seen (Figure 2a). Tropical easterly jet at around 16 km during
250 the Indian Summer Monsoon season (June-July-August) and semi-annual oscillation near the
251 stratopause (and at 80 km with different phase) are also clearly visible in the zonal winds (Figure
252 2b). Meridional winds do not exhibit any significant seasonal variation in the troposphere and
253 stratosphere but show large variability in the mesosphere (Figure 2c). These overall features in
254 the background temperature and wind match well with those reported considering data from
255 different instruments by Kishore Kumar et al., (2008 a,b).

256 The profiles of T obtained from MSISE-90 model and U and V from HWM-07 for 17
257 March 2012 are shown in Figure 3(a)-(c), respectively. The Gadanki model mean temperature
258 profile for the month of March and the temperature profile obtained from TIMED/SABER and
259 mean temperature obtained from ERA-Interim for the month of March 2012 are also
260 superimposed in Figure 3a for comparison. A very good agreement between the profiles can be

261 noticed. The profiles of U and V obtained from the Gadanki model for the month of March and
262 also monthly mean of the ERA-Interim are also superimposed in Figure 3b and 3c, respectively.
263 In general, a good match is seen between the Gadanki model and ERA-Interim and HWM-07
264 models up to the altitudes of stratopause. The differences between the two above the stratopause
265 could be due to tidal winds which have large amplitudes at mesospheric altitudes. Though tidal
266 amplitudes are already included in the HWM-07 model, their day-to-day variability may be
267 contributing to these differences. In order to avoid any bias due to day-to-day variability of the
268 tides at mesospheric altitudes, we have considered tidal amplitudes of 5 K, 10 K, 15 K and 10
269 m/s, 20 m/s, 30 m/s in temperature and winds, respectively, at 97 km to represent day-to-day
270 variability.

271 In general, troposphere is a highly dynamic region though the amplitudes of tides are
272 considerably low. In order to consider more realistic horizontal winds in the troposphere and
273 stratosphere, we further considered the ERA-Interim products (Dee et al., 2011). This data is
274 available at 6 h intervals with 1.5^0 x 1.5^0 grid resolution at 37 pressure levels covering from
275 surface (1000 hpa) to the stratopause (~1 hPa). The profiles of T, U and V from ERA-Interim for
276 17 March 2012 for 12 UTC are also superimposed in Figures 3(a), 3(b) and 3(c), respectively. In
277 general, good agreement between the other models and ERA-Interim model can be noticed
278 particularly in V in the lower and upper levels except between 10 and 20 km. Summarizing, we
279 have considered the following wind models: (1) ERA-Interim (from surface to 40 km) and HWM
280 07 models from 40-100 km, (2) Gadanki model, (3) zero wind (U=0 and V=0). Using these
281 background atmosphere profiles, we calculated the relevant atmospheric parameters like N^2 and
282 H. Profiles of T, U, and V obtained using ERA-interim data products for 8 March 2010, 6 UTC
283 over Hyderabad region are shown in Figures 3(c)-(f), respectively. T, U, and V profiles as

obtained from MSISE-90 and from HWM-07 for the same day are also provided in the respective panels. The background atmosphere information for wave events over Hyderabad is obtained in a manner similar to that mentioned above for Gadanki.

In order to calculate diffusive damping we used eddy diffusivity profiles for troposphere and lower stratosphere and mesosphere which are obtained using MST Radar (Narayana Rao et al., 2001) at Gadanki as shown in Figure 4a. In the altitude regions where there are data gaps, we extrapolated/interpolated the diffusivity profiles and the approximated profile with different analytical exponential functions is also shown in Figure 4a. The eddy diffusivity profile of Hocking's (Hocking, 1991) that is presented in Marks and Eckermann (1995) is also superimposed for comparison. Note that Hocking's profile corresponds mainly to mid latitudes. In general, eddy diffusivity is relatively higher in Hocking's profile than in the Gadanki profile. This same (Gadanki) profile is used for Hyderabad events also. In Figure 4b molecular diffusivity is shown. It is seen that the molecular diffusivity exceeds the eddy diffusivity at altitudes > 80 km. We have taken into account molecular diffusivity also in the ray tracing calculation while considering the total diffusivity above 80 km and the total diffusivity profile is shown in Figure 4b. Radiative and diffusive damping rates corresponding to Event G1 observed over Gadanki are shown in Figure 4c for illustration. It is seen that radiative damping rate is higher than the diffusive damping rate below 95 km. This is so for the other 13 events (G2-G5 and H1-H9) as well.

5. Application of reverse ray tracing for the wave events

By using the background parameters and the ray tracing equations, we trace back the ray path(s) to identify the GW source region(s). We used Runge-Kutta fourth order method for numerical integration at the time step of $\delta t = 100\ m/C_{gz}$ where 100 m is the height step

307 downwards from 97 km (the peak altitude of the airglow layer) and C_{gz} is the vertical group
308 velocity. As the ray tracing treatment is valid only when WKB approximation holds good, the
309 ray integration is terminated whenever the WKB approximation is violated. We terminated the
310 ray when 1) m^2 becomes negative, which means that the wave cannot propagate vertically, 2)
311 intrinsic frequency < 0 or approaching zero, which mean that the wave reached a critical layer
312 and is likely to break beyond this 3) WKB parameter approaching values greater than one
313 (beyond which WKB approximation breaks) and 4) vertical wave number becoming greater than
314 1 $x10^{-6}$ (approaching critical level) (Wrasse et al., 2006). Background wind in the direction of
315 wave propagation is checked with the horizontal phase speed of the wave and the ray integration
316 is terminated whenever it approaches the critical level. We calculated the wave action and thus
317 the amplitude along the ray path by including the damping mechanisms. As information on wave
318 amplitudes cannot be unambiguously determined from the optical emission intensity
319 measurements, we assumed the GW amplitude as unity (at 97 km) and traced back the relative
320 amplitudes along the ray path. Further, as we have not considered the local time variation of the
321 background parameters, the ground-based wave frequency will be a constant. However, note that
322 the intrinsic frequency still varies with altitude because of the varying background horizontal
323 winds.

324 The observed and calculated GW parameters (intrinsic frequency, wave period, zonal,
325 meridional, and vertical wave numbers) for all the wave events measured at the peak airglow
326 emission altitudes as described in Sections 2.1 and 2.2 are given as initial parameters to the ray
327 tracing code. We considered all the different combinations of observed wave parameters
328 including the errors in the observations for obtaining the ray paths and the uncertainties in them.
329 Note that atmospheric tides have large amplitudes in the MLT region which, at times, can be

330 comparable sometimes to those of the background wind. As mentioned earlier, though tidal
331 amplitudes are considered in the HWM-07 model, their day-to-day variability is not taken into
332 account in the model. Amplitudes of the tides may reach values as high as 20 m/s over equatorial
333 latitudes (Tsuda et al., 1999). As already mentioned we have included day to day variability of
334 tidal amplitudes into temperature and winds. In general, above the stratopause, tidal amplitudes
335 are large and increase exponentially with altitude. It is interesting to note that (figure not shown)
336 the variabilities in the background atmospheric parameters developed using data from a suite of
337 instruments as mentioned above lies within the variability due to tides. Ray path calculations are
338 also carried out for these background profiles.

339 We traced the ray path using the above initial parameters from the initial latitude
340 (13.5^{o}N/17.5^{o}N) and longitude (79.2^{o}E/78.5^{o}E) and altitude (97 km). The ray paths for the wave
341 events G1 with the longitude-altitude, latitude-altitude and longitude-latitude are shown in
342 Figures 5(a)-(c), respectively, for Gadanki and in Figures 5 (d)-(f) for (H1) Hyderabad. Ray
343 paths obtained while considering different background conditions (normal wind, zero wind and
344 Gadanki model wind) and the day-to-day variability of tides are also superimposed with dotted
345 lines. When we considered zero (Gadanki) wind, a shift of 71 km (25 km) in the horizontal
346 position of the terminal point is observed with respect to that for normal wind for wave event G1.
347 The shift reduced to 19 km and increased to 47 km and 97 km when we considered the tidal
348 variability of +5K, +10 m/s and +10 K, +20 m/s, +15 K, +30 m/s, respectively, with respect to
349 the normal wind. The shift is ~15 km for the tidal variability of -5 K, -10 m/s. The ray terminated
350 in the mesosphere itself for tidal variability of -10 K, -20 m/s and -15 K, -30 m/s (figure not
351 shown).

352 Over Hyderabad, for the wave event H1, shown in Figures 5(d)-(f), the shifts in the
353 horizontal location of the terminal point are 305.6 km (148.7 km) for tidal variability of +10, +20
354 m/s (-10 K, -20 m/s), respectively, with reference to zero wind. This difference is only 59.5 km
355 for tidal variability of -10 K, -20 m/s with respect to the normal wind. The terminal point
356 locations for the rest of the wave events for normal winds are listed in Table 1. Note that out of
357 the five wave events over Gadanki two wave events (G3 and G4) got terminated in the upper
358 mesosphere itself and one (G5) got terminated at 67 km. Over Hyderabad, out of the nine wave
359 events, two wave events (H4 and H7) got terminated at ~ 67 km. In general, all the wave events
360 which propagated down to the upper troposphere terminated between 10 and 14.5 km, except the
361 case G2 which got terminated at 17 km due violation of the WKB approximation. The violation
362 of the WKB approximation at 17 km could be due to sharp temperature gradients near
363 tropopause.

364 Profiles of square of vertical wave number (m^2), intrinsic frequency (ω_{ir}) and Brunt
365 Väiäsälä frequency (N), horizontal wavelength (λ_h), zonal, meridional, and vertical group speed
366 for the event G1 are shown in Figures 6(a)-(f), respectively. Profiles of these parameters obtained
367 for different background wind conditions (normal wind, zero wind, and Gadanki model wind)
368 and for the day-to-day variability of tides are also superimposed in the respective panels. The
369 differences with and without the variability of tides in the above mentioned parameters are small
370 below the stratopause, and are quite high above. Note that the effect of Doppler shifting of the
371 wave frequency is larger at higher altitudes due to higher wind amplitudes. Around 13 km, Brunt
372 Väisälä frequency is less than that of the intrinsic frequency and so the square of the vertical
373 wave number is negative there (Figure 6b). There is not much variation in the horizontal
374 wavelength with height (Figure 6c). Zonal group speed shows (Figure 6d) nearly the same

375 behaviour as that of the zonal wind. The intrinsic frequency, $\omega_{ir,}$ exceeded N at 13 km altitude
376 and due to this m^2 became negative and the ray path got terminated there. The observation time
377 at the ray-start and according times along the ray time shown in Figure 6(a) reveals that it has
378 taken 63 minutes.

379 As mentioned earlier, the information on the wave amplitudes is not available from the
380 observations. So we used the GW amplitude as unity (at the altitude of observation) and traced
381 back the relative amplitudes along the ray path. Profiles of amplitudes of GWs observed for the
382 wave events G1 and H1 over Gadanki and Hyderabad are shown in Figures 7(a) and 7(b),
383 respectively. Amplitudes with three different background wind conditions along with different
384 tidal amplitudes are also shown in the respective panels. Unit wave amplitude at the observed
385 region, translates to amplitude of 10^{-3} near the source region. Amplitude growth is found higher
386 when either Gadanki or zero wind models are considered and slightly lower for the normal wind.
387 The growth is highly reduced when tidal variability in the background wind is considered.
388 However, higher amplitude growth rates are obtained over Hyderabad when we considered
389 normal wind along with tidal variability than zero wind. Similar growth rates are also obtained
390 for other wave events (not shown). Thus, background winds play an important role in the growth
391 rates of GWs.

392 **6. Discussion on potential source(s) for the GW events**

393 The geographical locations of the terminal points for different combinations of
394 background winds along with different combinations of tidal variability are shown in Figures 8
395 and 9 for Gadanki and Hyderabad wave events, respectively. In this figure, the contour
396 encircling all the points (not drawn in the panels of the figure) represents the horizontal spread of
397 uncertainty due to background conditions (including tidal variability). Terminal point of the ray

398 (in the troposphere) is expected to be the location of GW source. Since 9 out of 14 wave events
399 got terminated between 10 and 17 km, we search for the possible sources around this altitude at
400 the location. In general, major sources for the GW generation over tropics are orography,
401 convection, and vertical shear in the horizontal winds. In the present case, GWs are unlikely to
402 be orographic origin as the observed waves have phase speeds much greater than zero. Tropical
403 deep convection is assumed to be a major source for the generation of wide spectrum of GWs in
404 the tropical latitudes. As mentioned earlier, OLR/IR BT is assumed to be proxy for the tropical
405 deep convection. Lower the OLR/BT values, higher the cloud top and hence the deeper the
406 convection. OLR (IRBT) < 240 W/m^2 (K) is taken to represent deep convection. However,
407 convection may exist at locations away from the observational site and waves generated at those
408 locations can propagate to the mesospheric altitudes over the site. In order to see the presence or
409 otherwise of convection in the vicinity of the termination location, latitude-longitude cross
410 section of NOAA interpolated OLR obtained for 17 March 2012 (8 March 2010) is shown in
411 Figure 8a (Figure 9a) for Gadanki (Hyderabad) region. The terminal points of the rays for the
412 wave events G1 and G2 (H1-H9 except H4 and H7) with different background wind conditions
413 and different combinations of variability of the tides are also shown in the figure. As expected,
414 no convection in-and-around Gadanki (Hyderabad) region can be noticed in this figure. Note that
415 this plot is with a coarse grid (2.5^o x 2.5^o latitude-longitude) averaged for a day. The observed
416 GWs could be generated due to localized sources having shorter temporal and spatial scales than
417 those seen from the NOAA OLR data used. In order to examine this, we have used IR BT data
418 which is available at 4 km x 4 km grid size and at half an hour basis. Latitude and longitude
419 section of hourly IR BT at 14 UTC (10 UTC), 15 UTC and 16 UTC is shown in Figures 8(b)-(d)
420 (Figure 9b), respectively. The terminal points with and without variability of the tides are also

421 shown. Interestingly no cloud patches are seen at any of the times mentioned above. Thus,
422 convection as a possible source for the observed wave events can be ruled out.

423 The other possible source for GW generation is the vertical shear in the horizontal wind.
424 The vertical shear in horizontal winds at an altitude of 10 km (8 km) on 17 March 2012 (8 March
425 2010) as a function of latitude-longitude is shown in Figure 10a (Figure 10b). The terminal
426 points of the rays for both the wave events with and without the day-to-day variability of the
427 tides are also shown in the figure. Interestingly, at all the terminal points (in the troposphere),
428 strong vertical shear in the horizontal wind which is quite high (8-9 m/s/km) is seen. In order to
429 see whether these waves could be generated due to non-linear interaction (through Kelvin
430 Helmholtz Instability, KHI), the Richardson number ($Ri = \frac{N^2}{(dU/dz)^2}$) for the nearest location
431 is calculated (using nearby radiosonde data) and is shown in Figure 11. From figure it can be
432 noticed that Ri is < 0.25 showing that Ri satisfies the condition for instability for the observed
433 waves at both the stations. Thus, the shear is unstable and hence conducive for the excitation of
434 KHI leading to the generation of the propagating GWs through non-linear interaction. Note that
435 shear excitation of the GWs has been examined theoretically using both linear and non-linear
436 approaches (e.g., Fritts, 1982; 1984; McIntyre, 1978). For the excitation of radiating GWs by KH
437 instabilities at a shear layer, the two mechanisms that are examined are the vortex pairing (sub-
438 harmonic interaction) and envelope radiation (Fritts, 1984). The vortex pairing is found to be
439 highly dependent on the minimum Ri, whereas, the envelope radiation mechanism is found to
440 provide efficient radiating wave excitation in the absence of propagating unstable modes (Fritts,
441 1984). Theoretical and numerical simulation work needs to be carried out to examine which of
442 these mechanisms is effective for the observed events in the present study. This aspect is beyond
443 the scope of the present study and is planned to be taken up in the future.

444 Note that five wave events terminated at mesospheric altitudes. We examined the
445 background atmospheric condition which can lead to the termination for these wave events at
446 such high altitudes. The ray paths for two wave events observed on the same day over Gadanki
447 could propagate down below with the same background atmosphere. When wave parameters
448 related to this event are examined (Table 1) it can be seen that the phase speeds are small when
449 compared to the other two wave events. When the wave is introduced at around 15 km with all
450 the wave parameters similar to that observed at 97 km for this event and forward ray tracing is
451 carried out, it is seen that the ray propagated up to 50 km terminating there. Note that strong
452 vertical shear in the background wind is seen at this altitude (Fig. 3). To investigate the role of
453 shear in the process of propagation of waves, the shear is reduced to almost 0 in the 50 – 80 km
454 altitude region. Under such conditions this wave event also could propagate to ~16 km (in the
455 reverse ray tracing). This reveals that the background wind shear is obstructing the ray path. It is
456 quite likely that the wave got ducted between 50 and 80 km and similar results are obtained for
457 the other cases which got terminated in the mesosphere. This indicates that wind shears at
458 mesospheric altitudes are responsible for termination at mesospheric altitudes for these events.

459 **7. Summary and conclusions**

460 Identification of the GW sources for the 14 wave events observed over Gadanki and
461 Hyderabad using optical airglow measurements is presented. Reverse ray tracing method is
462 developed to obtain the location of the source regions of the GWs in the
463 troposphere/mesosphere. We made use of the MSISE-90 model for temperature and the HWM-
464 07 for the zonal and meridional winds in addition to the ERA-Interim products in the lower
465 atmosphere (1000 hPa to 1 hPa pressure levels), Gadanki climatological model, and zero wind
466 model for the background atmosphere. We have incorporated also the expected variability of

467 tidal amplitudes of 5 K, 10 K, 15 K and 10 m/s, 20 m/s, 30 m/s in temperature and winds,
468 respectively. The terminal points lie in the range of 50-100 km and 60-300 km for Gadanki and
469 Hyderabad, respectively when different wind and tidal variabilities are used. Wave action is
470 successfully implemented taking into account the radiative and diffusive damping. Considering
471 the wave amplitude as unity at 97 km, amplitude of the wave is traced back to the source region
472 for different wind models. Out of the 14 events examined, 9 ray paths terminated in the
473 troposphere. The remaining 5 events got terminated in the mesosphere itself. We examined for
474 possible sources for the 9 events for which the ray paths terminated in the troposphere.

475 Orography as the possible source was ruled out as wave events have high phase speeds.
476 No tropical deep convection in-and-around Gadanki and Hyderabad was noticed near the ray
477 terminal points. Interestingly, strong vertical shear in the horizontal wind is observed near the
478 terminal points and these large shears are attributed to be the source for the GW events observed
479 at the mesospheric altitudes. Preusse et al., (2008) discussed the transparency of the waves to the
480 atmosphere in different seasons. They reported that during equinox times atmosphere is more
481 transparent to the high phase speed and shorter horizontal wavelength waves than that in the
482 solstices. Waves with shorter (<10 km) hhorizontal wavelengths tend to be removed by vertical
483 reflection or evanescence at the source and slower phase speeds are more prone to critical level
484 removal. This leads to a preference for waves with longer horizontal wavelengths and faster
485 ground-based phase speeds to reach the MLT. However, they observed that many rays penetrated
486 to the MLT at the tropical latitude where wind speed is low in comparison to the mid and high
487 latitudes. In our case, whenever phase speed is low for short horizontal wavelength waves, ray
488 didn't reach up to the troposphere and it got stopped at mesospheric altitude itself. While there is
489 strong evidence for convectively generated gravity waves, evidence for tropospheric wind shear

generated GWs is rather sparse (Mastrantonio 1976; Fritts and Alexander 2003). The present study clearly demonstrated that high frequency high phase speed GWs observed in the mesosphere can be generated by tropospheric wind shear. Examination of the background wind conditions and wave parameters for the events that got terminated in the mesosphere revealed that the phase speeds were quite low for these strong vertical shears in the 50-80 km region (and at 95 km) resulted in the termination of the ray paths. It is likely that the waves generated in the troposphere are ducted between 50-80 km and the waves observed above this region are due to leakage of waves from the duct. It is also likely that the observed GWs in these cases (G3, G4, G5, H5 and H7) are from secondary wave generation due to wave breaking at the termination region. While secondary wave generation due to convectively generated waves has been investigated (e.g. Zhou et al., 2002; Chun and Kim 2008) such investigations have not yet been carried out for GWs of shear origin. This aspect needs further investigation. Note that we have tested reverse ray tracing method successfully for fourteen wave events. Further, wave action is also implemented successfully by assuming the wave amplitudes as unity as information on the same is not available from optical observations. However, more number of cases are needed to be examined, particularly for the events that occur during Indian Summer Monsoon season where convection and strong vertical shears in the horizontal winds co-exist due to prevailing tropical easterly jet (Venkat Ratnam et al., 2008). A few experiments are planned to be conducted at Gadanki by operating simultaneously MST radar, Radiosonde, Rayleigh Lidar, Airglow imager and Meteor radar which provides information right from the troposphere to the MLT region. Note that such a study on the vertical propagation of meso-scale gravity wave from lower to upper atmosphere was made recently by Shin Suzuki et al. (2013) using Airglow Imager and Lidar over Arctic region.

513 **Acknowledgements:** This work is done as a part of SAFAR and CAWSES India phase II
514 programs. We thank NARL staff for providing data used in the present study. We deeply
515 appreciate NOAA, HWM-07, ERA-Interim for providing data used in the present study through
516 their ftp sites. This work is supported by Department of Space, Government of India.
517

518 **References**

519 Alexander, M. J., J. R. Holton, and D. R. Durran (1995), The gravity wave response above deep
520 convection in a squall line simulation. J. Atmos. Sci., 52, 2212-2226.

521 Alexander , M. J., M. Geller, C. McLandress, S. Polavarapu, P. Preusse, F. Sassi, K. Sato, S.
522 Eckermann, M. Ern, A. Hertzog, Y. Kawatani, M. Pulido, T. A. Shaw, M.Sigmond, R. Vincent
523 and S. Watanabe (2010), Recent developments in gravity-wave effects in climate models, and
524 the global distribution of gravity-wave momentum flux from observations and models, Q. J. R.
525 Meteorol. Soc. 136: 1103–1124.

526 Brown, L. B., A. J. Gerrard, J. W. Meriwether, J. J. Makela (2004), All-sky imaging
527 observations of mesospheric fronts in OI 557.7 nm and broadband OH airglow emissions:
528 Analysis of frontal structure, atmospheric background conditions, and potential sourcing
529 mechanisms, J. Geophys. Res., 109, D19104, doi:10.1029/2003JD004223.

530 Chun, H.Y., Y.H. Kim (2008), Secondary waves generated by breaking of convective gravity
531 waves in the mesosphere and their influence in the wave momentum flux, J. Geophys. Res.,
532 113, D23107, doi:10.1029/2008JD009792, 2008.

533 Clark, T. L., T. Hauf, and J. P. Kuettner (1986), Convectively forced internal gravity waves:
534 Results from two-dimensional numerical experiments, Q. J. R. Meteorol. Soc., 112, 899– 925,
535 doi:10.1002/qj.49711247402.

536 Debashis Nath., M. Venkat Ratnam, V. V. M. Jagannadha Rao, B. V. Krishna Murthy, and S.
537 Vijaya Bhaskara Rao (2009), Gravity wave characteristics observed over a tropical station
538 using high-resolution GPS radiosonde soundings, J. Geophys. Res., 114, D06117,
539 doi:10.1029/2008JD011056.

540 Dee, D. P., S. M. Uppala, A. J. Simmons, P. Berrisford, P. Poli, S. Kobayashi, U. Andrae, M. A.

541 Balmaseda, G. Balsamo, P. Bauer, P. Bechtold, A. C. M. Beljaars, L. van de Berg, J. Bidlot, N.
542 Bormann, C. Delsol, R. Dragani, M. Fuentes, A. J. Geer, L. Haimberger, S. B. Healy, H.
543 Hersbach, E. V. Hólm, L. Isaksen, P. Kållberg, M. Köhler, M. Matricardi, A. P. McNally, B. M.
544 Monge-Sanz, J.-J. Morcrette, B. K. Park, C. Peubey, P. de Rosnay, C. Tavolato, J.-N. Thépaut
545 and F. Vitart (2011), The ERA-Interim-reanalysis: configuration and performance of the data
546 assimilation system, Q. J. R. Meteorol. Soc.137: 553 – 597.
547 Dhaka, S. K., R. K. Choudhary, S. Malik, Y. Shibagaki, M. D. Yamanaka, and S. Fukao (2002),
548 Observable signatures of a convectively generated wave field over the tropics using Indian
549 MST radar at Gadanki (13.5^{o}N, 79.2^{o}E), Geophys. Res. Lett., 29(18), 1872,
550 doi:10.1029/2002GL014745.
551 Drob, D.P., J. T. Emmert, G. Crowley, J. M. Picone, G. G. Shepherd, W. Skinner, P. Hays, R. J.
552 Niciejewski, M. Larsen, C. Y. She, J. W. Meriwether, G. Hernandez, M. J. Jarvis, D. P. Sipler,
553 C. A. Tepley,M. S. O'Brien, J. R. Bowman, Q. Wu, Y. Murayama, S. Kawamura, I. M. Reid
554 and R. A. Vincent (2008), An empirical model of the Earth's horizontal wind fields: HWM07,
555 J. Geophys. Res., 113, A12304, doi:10.1029/2008JA013668.
556 Dutta, G., M. C. Ajay Kumar, P. Vinay Kumar, M. Venkat Ratnam, M. Chandrashekar, Y.
557 Shibagaki, M. Salauddin, and H. A. Basha (2009), Characteristics of high-frequency gravity
558 waves generated by tropical deep convection: Case studies, J. Geophys. Res., 114, D18109,
559 doi:10.1029/2008JD011332.
560 Eckermann, S. D., and P. Preusse (1999), Global Measurements of Stratospheric Mountain
561 Waves from space, Science., 286.
562 Fovell, R., D. Durran, and J. R. Holton (1992), Numerical simulations of convectively generated
563 stratospheric gravity waves. J. Atmos. Sci., 49, 1427-1442.

564 Fritts, D.C (1982), Shear Excitation of Atmospheric Gravity Waves. J. Atmos. Sci., 39, 1936-
565 1952.
566 Fritts, D.C, (1984), Shear Excitation of Atmospheric Gravity Waves, Part II: Nonlinear
567 Radiation from a Free Shear Layer, J. Atmos. Sci., 41, 524-537.
568 Fritts, D.C., M.J. Alexander (2003), Gravity wave dynamics and effects in the middle
569 atmosphere. Reviews of Geophysics 41 (1), doi: 10.1029/2001RG000106.
570 Fritts, D.C., Sharon L. Vadas, Kam Wan, Joseph A. Werne (2006), Mean and variable forcing of
571 the middle atmosphere by gravity waves, J. Atmos. and Sol. Terr. Phys., 68, 247–265.
572 Geller, M.A., M.J. Alexander, P.T. Love, J. Bacmeister, M. Ern, A. Hertzog, E. Manzini, P.
573 Preusse, K. Sato, A. Scaife, and T. Zhou (2013), A comparison between gravity wave
574 momentum fluxes in observations and climate models. J. Climate, 26, 6383-6405,
575 doi:10.1175/JCLI-D-12-00545.1.
576 Gerrard, A.J., Timothy J. Kane, Stephen D. Eckermann, and Jeffrey P. Thayer (2004), Gravity
577 waves and mesospheric clouds in the summer middle atmosphere: A comparison of lidar
578 measurements and ray modeling of gravity waves over Sondrestrom, Greenland, J. Geophys.
579 Res., 109, D10103, doi:10.1029/2002JD002783.
580 Guest, F.M., M.J. Reeder, C.J. Marks, D.J. Karoly (2000),Inertia–Gravity Waves Observed in
581 the Lower Stratosphere over Macquarie Island, J. Atmos. Sci., 57.
582 Hecht, J.H., R.L. Walterscheid, M.N. Ross (1994), First measurements of the two-dimensional
583 horizontal wave number spectrum from CCD images of the nightglow. J. Geophys. Res., 99
584 (A6), 11449–11460.
585 Hedin, A.E (1991), Extension of the MSIS Thermosphere model into the middle and Lower
586 atmosphere, J. Geophys. Res., 96, NO. A2, 1159-117.

587 Hertzog, A., C. Souprayen, and A. Hauchecorne (2001), Observation and backward trajectory of
588 an inertio-gravity wave in the lower stratosphere, Annales Geophysicae., 19, 1141–1155.
589 Hocking, W.K., (1991), The effects of middle atmosphere turbulence on coupling between
590 atmospheric regions, J. Geomag., Geoelc., 43 (sup), 621-636.
591 Janowiak, J.E., R.J. Joyce, and Y. Yarosh (2001), A real-time global half-hourly pixel-resolution
592 IR dataset and its applications. Bull. Amer. Meteor. Soc., 82, 205-217.
593 Jones, W.L (1969), Ray tracing for internal gravity waves. J. Geophys. Res., 74 (8), 2028–2033.
594 Kumar, K. K. (2006), VHF radar observations of convectively generated gravity waves: Some
595 new insights, Geophys. Res. Lett., 33, L01815, doi:10.1029/2005GL024109.
596 Kumar, K. K. (2007), VHF radar investigations on the role of mechanical oscillator effect in
597 existing convectively generated gravity waves, Geophys. Res. Lett., 34, L01803,
598 doi:10.1029/2006GL027404.
599 Kishore Kumar, G., M. Venkat Ratnam, A. K. Patra, S. Vijaya Bhaskara Rao, and J. Russell
600 (2008a), Mean thermal structure of the low-latitude middle atmosphere studied using Gadanki
601 Rayleigh lidar, Rocket, and SABER/TIMED observations, J. Geophys. Res., 113, D23106,
602 doi:10.1029/2008JD010511.
603 Kishore Kumar, G., M. Venkat Ratnam, A. K. Patra, V. V. M. Jagannadha Rao, S. Vijaya
604 Bhaskar Rao, K. Kishore Kumar, S. Gurubaran, G. Ramkumar, and D. Narayana Rao (2008b),
605 Low-latitude mesospheric mean winds observed by Gadanki mesosphere-stratosphere-
606 troposphere (MST) radar and comparison with rocket, High Resolution Doppler Imager
607 (HRDI), and MF radar measurements and HWM93, J. Geophys. Res., 113, D19117,
608 doi:10.1029/2008JD009862.

609 Laskar, F. I., D. Pallamraju, T. Vijaya Lakshmi, M. Anji Reddy, B. M. Pathan, and S.
610 Chakrabarti (2013), Investigations on vertical coupling of atmospheric regions using combined
611 multiwavelength optical dayglow, magnetic, and radio measurements, J. Geophys. Res. Space
612 Physics, 118, 4618-4627, doi:10.1002/jgra.50426.
613 Lilly, D. K., and P. J. Kennedy (1973), Observations of a stationary mountain wave and its
614 associated momentum flux and energy dissipation. J. Atmos. Sci., 30, 1135-1152.
615 Mastrantonio, G., F. Einaudi, D. Fua, and D. P. Lalas (1976), Generation of gravity waves by jet
616 streams in the at-mosphere, J. Atmos. Sci., 33, 1730-1738.
617 Marks, C.J., S.D. Eckermann (1995), A three-dimensional non-hydrostatic ray-tracing model for
618 gravity waves: formulation and preliminary results for the middle atmosphere. J. Atmos. Sci.,
619 52 (11), 1959–1984.
620 McIntyre, M.E., and M. A. Weissman (1978), On Radiating Instabilities and resonant over-
621 reflection. J. Atmos. Sci., 35, 1190-1196.
622 Nakamura, T., T. Aono, T. Tsuda, A.G. Admiranto, E. Achmad Suranto (2003), Mesospheric
623 gravity waves over a tropical convective region observed by OH airglow imaging in Indonesia.
624 Geophysical Research Letters 30 (17), 1882–1885.
625 Narayana Rao, D., M. V. Ratnam, T. N. Rao, S. V. B. Rao (2001), Seasonal variation of vertical
626 eddy diffusivity in the troposphere,lower stratosphere and mesosphere over a tropical station.
627 Annales Geophysicae , 19.
628 Nastrom, G.D., D.C. Fritts (1992), Sources of mesoscale variability of gravity waves I:
629 topographic excitation. J. Atmos. Sci., 49 (2), 101–110.
630 O'Sullivan,D., and T.J. Dunkerton (1995), Generation of Inertia Gravity waves in a simulated
631 life cycle of Baroclinic Instability, J. Atmos. Sci., 52(21).

632 Pallamraju, D., F. I. Laskar, R. P. Singh, J. Baumgardner, and S. Chakrabarti (2013), MISE: A
633 Multiwavelength Imaging Spectrograph using Echelle grating for daytime optical agronomy
634 investigations, J. Atmos. Sol-Terr. Phys., 103, 176 - 183.
635 Pallamraju, D., J. Baumgardner, R. P. Singh, F. I. Laskar, C. Mendillo, T. Cook, S. Lockwood,
636 R. Narayanan, T. K. Pant, and S. Chakrabarti (2014), Daytime wave characteristics in the
637 mesosphere lower thermosphere region: Results from the Balloon-borne Investigations of
638 Regional-atmospheric Dynamics experiment, J. Geophys. Res. Space Physics, 119 (3),
639 doi: 10.1002/2013JA019368.
640 Pfister, L., K.R. Chan, T.P. Bui, S. Bowen, M. Legg, B. Gary, K. Kelly, M. Proffitt, and W. Starr
641 (1993), Gravity Waves Generated by a Tropical Cyclone During the STEP Tropical
642 Field Program: A Case Study, J. Geophys. Res., 98, D5.
643 Piani, C., D. Durran, M. J. Alexander, and J. R. Holton (2000), A numerical study of three-
644 dimensional gravity waves triggered by deep tropical convection and their role in the dynamics
645 of the QBO, J. Atmos. Sci., 57, 3689 – 3702, doi:10.1175/1520-0469(2000)057<3689.
646 Plougonven, R., and F. Zhang (2014), Internal gravity waves from atmospheric jets and fronts,
647 *Rev. Geophys.*, *52*, 33–76, doi:10.1002/2012RG000419.
648 Preusse. P., S. D. Eckermann and M. Ern (2008), Transparency of the atmosphere to short
649 horizontal wavelength gravity waves, J. Geophys. Res., 113, D24104,
650 doi:10.1029/2007JD009682.
651 Queney, P., (1948), The problem of air flow over mountains: A summary of theoretical results,
652 Bull. AMS., 29, 16-26.
653 Salby, M. L., R.R. Garcia (1987), Transient response to localized episodic heating in the Tropics,
654 Part1: Excitation and short- time Near field behavior, J. Atmos. Sci., 44(2).

655 Schoeberl, M. R (1985), A ray tracing model of gravity wave propagation and breakdown in the
656 middle atmosphere, J. Geophys. Res., 90, 7999-8010, DOI: 10.1029/JD090iD05p07999.
657 Shin Suzuki, Franz-JosefLubkena, Gerd Baumgarten, Natalie Kaifler, Ronald Eixmann, Bifford
658 P. Williams, Takuji Nakamura (2013), Vertical propagation of a mesoscale gravity wave from
659 the lower to the upper atmosphere, J. Atmos. Sol. Terr. Phys., 97, 29–36.
660 Taori, A., A. Jayaraman, V. Kamalakar (2013), Imaging of mesosphere–thermosphere airglow
661 emissions over Gadanki (13.5 ^{0}N, 79.2 ^{0}E)—first results, J. Atmos. and Sol. Terres. Phys. 93,
662 21-28.
663 Taylor, M.J., W.R.J. Pendleton, S. Clark, H. Takahashi, D. Gobbi, R.A. Goldberg (1997), Image
664 measurements of short-period gravity waves at equatorial latitudes. Journal of Geophysical
665 Research., 102 (D22), 26283–26299.
666 Toshitaka Tsuda, Kazunori Ohnishi, Fusako Isoda, Takuji Nakamura, Robert A. Vincent, Iain M.
667 Reid, Sri Woro B. Harijono, Tien Sribimawati, Agus Nuryanto, Harsono Wiryosumarto (1999),
668 Coordinated radar observations of atmospheric diurnal tides in equatorial regions. Earth Planets
669 Space., 51, 579–592
670 Vadas, S.L., M. J. Taylor, P.-D. Pautet, P. A. Stamus, D. C. Fritts, H.-L. Liu, F. T. S˜ao Sabbas,
671 V. T. Rampinelli, P. Batista, and H. Takahashi (2009), Convection: the likely source of the
672 medium-scale gravity waves observed in the OH airglow layer near Brasilia, Brazil, during the
673 SpreadFEx campaign, Ann. Geophys., 27, 231–259.
674 Venkat Ratnam, M., A. Narendra Babu, V. V. M. Jagannadha Rao, S. Vijaya Baskar Rao, and D.
675 Narayana Rao (2008), MST radar and radiosonde observations of inertia-gravity wave
676 climatology over tropical stations: Source mechanisms, J. Geophys. Res., 113, D07109,
677 doi:10.1029/2007JD008986.

678 Vincent, R. A., and M. J. Alexander (2000), Gravity waves in the tropical lower stratosphere: An
679 observational study of seasonal and interannual variability, J. Geophys. Res., 105, 17,971-
680 17,982.
681 Wrasse, C.M., T. Nakamura, T. Tsuda, H. Takahashi, A.F. Medeiros, M.J. Taylor, D. Gobbi, A.
682 Salatun, Suratno, E. Achmad, A.G. Admiranto (2006), Reverse ray tracing of the mesospheric
683 gravity waves observed at 23°S (Brazil) and 7°S (Indonesia) in airglow imagers, J. Atmos.
684 Sol. Terr. Phys., 68, 163–181.
685 Zhou, X.L., J.R. Holton.,G.L. Mullendore (2002), Forcing of secondary waves by breaking of
686 gravity waves in the mesosphere, J. Geophys. Res., 107, NO. D7, 4058,
687 10.1029/2001JD001204.
688 Zhu, X., (1993), Radiative damping revisited: Parameterization of damping rate in the middle
689 atmosphere, J. Atmos. Sci., 50, 3008-3012.
690

691 **Figure captions:**

692 **Figure 1**. Identification of three wave events (left to right) obtained from the airglow emission
693 intensities originating from O(^{1}S) emissions from Gadanki. The wave crests are emphasized by
694 yellow freehand lines. Motion of waves can be obtained by successive images and the
695 direction of propagation is shown by red arrows. Time of occurrence of events is shown in
696 each image in UT (hh:mm).

697 **Figure 2**. Climatological monthly mean contours of (a) temperature, (b) zonal wind and (c)
698 meridional wind obtained over Gadanki region combining a variety of instruments listed in
699 Table 2.

700 **Figure 3**. Profiles of (a) temperature (b) zonal wind and (c) meridional wind obtained using
701 ERA-interim data products for 17 March 2012, 12 UTC over Gadanki region. Profiles obtained
702 from variety of sources over Gadanki (Gadanki model) listed in Table 2 are also superimposed
703 in the respective panels for comparison. Plots (d)-(e) are same as (a)-(c) but obtained for
704 Hyderabad on 8 March 2010. Temperature profile obtained from MSISE-90 and zonal and
705 meridional winds obtained from HWM 07 for the same day are also provided in the respective
706 panels.

707 **Figure 4**. (a) Profile of eddy diffusitvity (thick red line) obtained from Gadanki MST radar (Rao
708 et al., 2001) in the tropopshere, lower stratopshere and mesopshere. Fitted profile (dotted line)
709 with exponetial function is also shown. Hocking's (Hocking 1991) analytical curve
710 (extrapolated) is also superimposed for comparsion. (b) Profiles of eddy, molecualr, and total
711 diffusivity. (c) radiative, and diffusive damping rates.

712 **Figure 5**. Ray paths for the wave event G1 (started at 97 km) in the (a) Longitude-Altitude, (b)
713 Latitude-Altitude, and (c) Longitude-Latitude cross sections. Ray paths obtained while

considering different background wind conditions (normal wind, zero wind and Gadanki model wind) and the day-to-day variability of tides are also superimposed (dotted lines). (d)-(f) same as (a)-(c) but for the wave event H1. Note that Gadanki atmospheric model wind is not used for the wave events over Hyderabad.

Figure 6. Profiles of (a) square of vertical wave number (m^2), (b) intrinsic frequency (ω_{ir}) and Brunt Väisälä frequency (N) (green), (c) horizontal wavelength (d) zonal, (e) meridional, and (f) vertical group velocities for the wave event G1. Profiles of the same obtained while considering the three different background winds (different colored lines) and the day-to-day variability of tides are also superimposed (dotted lines) in the respective panels. The observation time at the ray-start and according times along the ray time is also shown in (a) with axis on the top.

Figure 7. Normalised amplitudes of gravity waves observed for the wave events (a) G1, and (b) H1, over Gadanki and Hyderabad, respectively. Amplitudes with three different background wind conditions along with different tidal amplitudes are also shown.

Figure 8. Daily mean latitude-longitude section of (a) OLR observed using NOAA products over Indian region on 17 March 2012. (b)-(d) same as (a) but for IRBT observed at 14 UTC, 15 UTC, and 20 UTC, respectively. Open (closed) circles in (a) (b-d) depict the terminal points of the ray paths shown in Figure 4.

Figure 9. Same as Figure 8 but for wave events observed over Hyderabad on 8 March 2010. Note that IRBT is shown only for 10 UTC.

Figure 10. Latitude-longitude section of vertical shear in the horizontal wind observed using ERA-Interim data products on (a) 17 March 2012 at 10 km, (b) 8 March 2010 at 8 km. Filled

736 circles depicts the terminal points of the ray paths estimated using three different wind
737 conditions and tidal amplitudes.
738 **Figure 11**. Profiles of Richardson number calculated close to the termination point using
739 radiosonde data for (a) VOMM (Gadanki) and (b) Goa (Hyderabad) locations.
740
741
742
743 **Table captions:**
744 **Table 1**. GW characteristics (direction of propagation (φ), horizontal wavelength (λ_h), period
745 (T), phase speed (C) and intrinsic frequency (ω_{ir})) for events observed over Gadanki (G) and
746 Hyderabad (H). The terminal point locations (latitude, longitude and altitude) are also shown
747 for each event. Conditions leading to the termination for each wave event are also shown.
748 Events for which ray paths terminated at mesospheric altitude are indicated with an asterisk.
749 **Table 2.** Details of instruments, parameters measured, altitude range in which data is available
750 and the duration of the data considered for developing the Gadanki atmospheric model.

751 **Tables:**

Events	φ (degrees)	Λh (km)	T (min)	C (m/s)	Longitude (degrees)	Latitude (degrees)	Altitude (km)	ω_{ir} (rad/s)	Termination condition
Gadanki location									
G1	102	85 (26)	18	78	79.9	10.8	13	0.00058	m^2 <0
G2	98	34 (28.9)	9	63	79.4	12.3	17	0.0116	WKB > 1
G3	132	12 (13.6)	6	33	79.2	13.37	96.9*	0.0006	Intrinsic frequency approaching zero
G4	62	134 (40)	12	186	79.14	13.2	92.9*	0.0093	WKB >1
G5	142	16 (2)	8	33	79.9	12.7	66.9*	0.0156	WKB >1 and m^2<0
Hyderabad location									
H1	11	39 (23.7)	16	41	70.2	15.8	10.5	0.0028	WKB >1
H2	16	57 (31.5)	16	59	75.3	16.4	13.5	0.0046	WKB >1
H3	21	74 (39)	16	77	75.9	16.3	14.5	0.0049	WKB >1
H4	11	39 (19.6)	20	32.5	76.3	17.1	67.6*	0.00083	m^2 > limiting condition and intrinsic frequency approaching zero
H5	16	57 (25)	20	48	72.7	15.7	12.5	0.0029	WKB >1
H6	21	74 (31)	20	61.7	74.7	15,8	13.5	0.0035	WKB >1
H7	11	39 (17.7)	23	28	75.8	16.9	68.5*	0.00087	m^2 > limiting condition and intrinsic frequency approaching zero
H8	16	57 (23)	23	41	68.3	14,8	11.5	0.0022	WKB >1
H9	21	74 (27)	23	54	73.4	15.4	13.5	0.0032	WKB >1

752 **Table 1**. GW characteristics (direction of propagation (φ), horizontal wavelength (λ_h) (vertical wavelength (λ_z)), period (T), phase
753 speed (C) and intrinsic frequency (ω_{ir})) for events observed over Gadanki (G) and Hyderabad (H). The terminal point locations
754 (latitude, longitude and altitude) are also shown for each event. Conditions leading to the termination for each wave event are also
755 shown. Events for which ray paths terminated at mesospheric altitude are indicated with an asterisk.

Instrument (parameter(s) obtained)	**Altitude range covered**	**Duration of the data considered**
Indian MST radar (U,V)	4-21 km and 65-85 km	1996-2012
Radiosonde (U, V, T)	1-30 km	2006- 2012
Lidar (T)	30-75 km	1998- 2012
Rocket (U, V, T)	22-80 km	1970-1991, 2002-2007
HALOE, HRDI / UARS (T, U, V)	65-110 km	1991- 2000
SABER/TIMED (T)	30-110 km	2002-2012

Table 2. Details of instruments, parameters measured, altitude range in which data is available and the duration of the data considered for developing the Gadanki atmospheric model.

Figures:

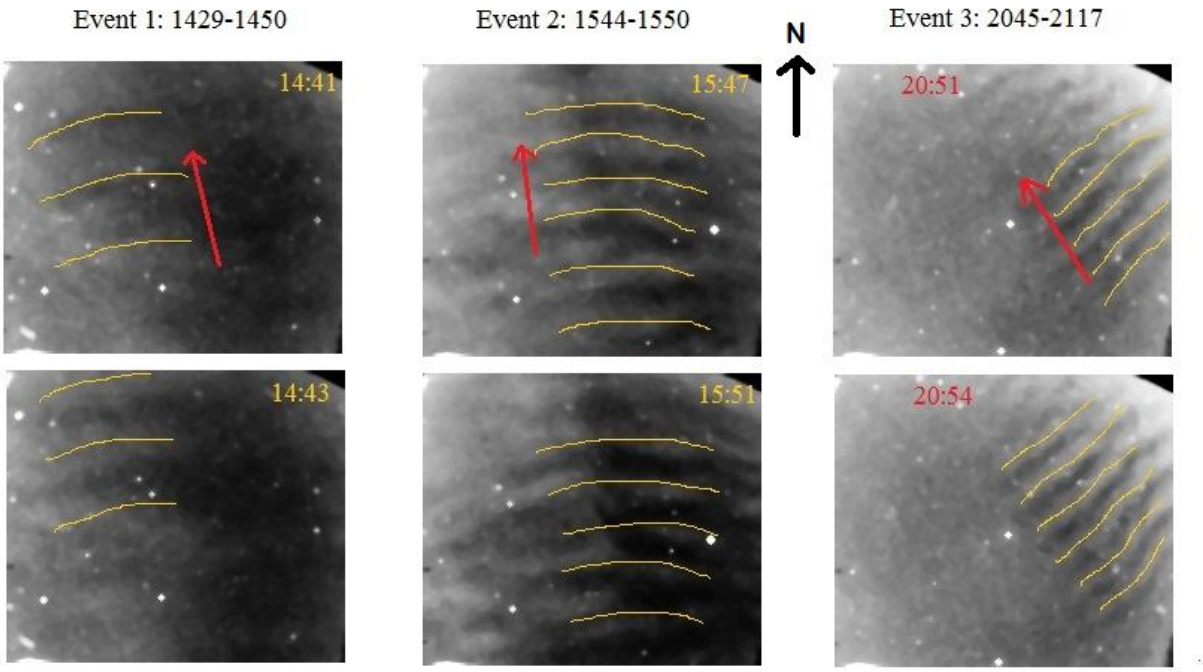

Figure 1. Identification of three wave events (left to right) obtained from the airglow emission intensities originating from O(^{1}S) emissions from Gadanki. The wave crests are emphasized by yellow freehand lines. Motion of waves can be obtained by successive images and the direction of propagation is shown by red arrows. Time of occurrence of events is shown in each image in UT (hh:mm).

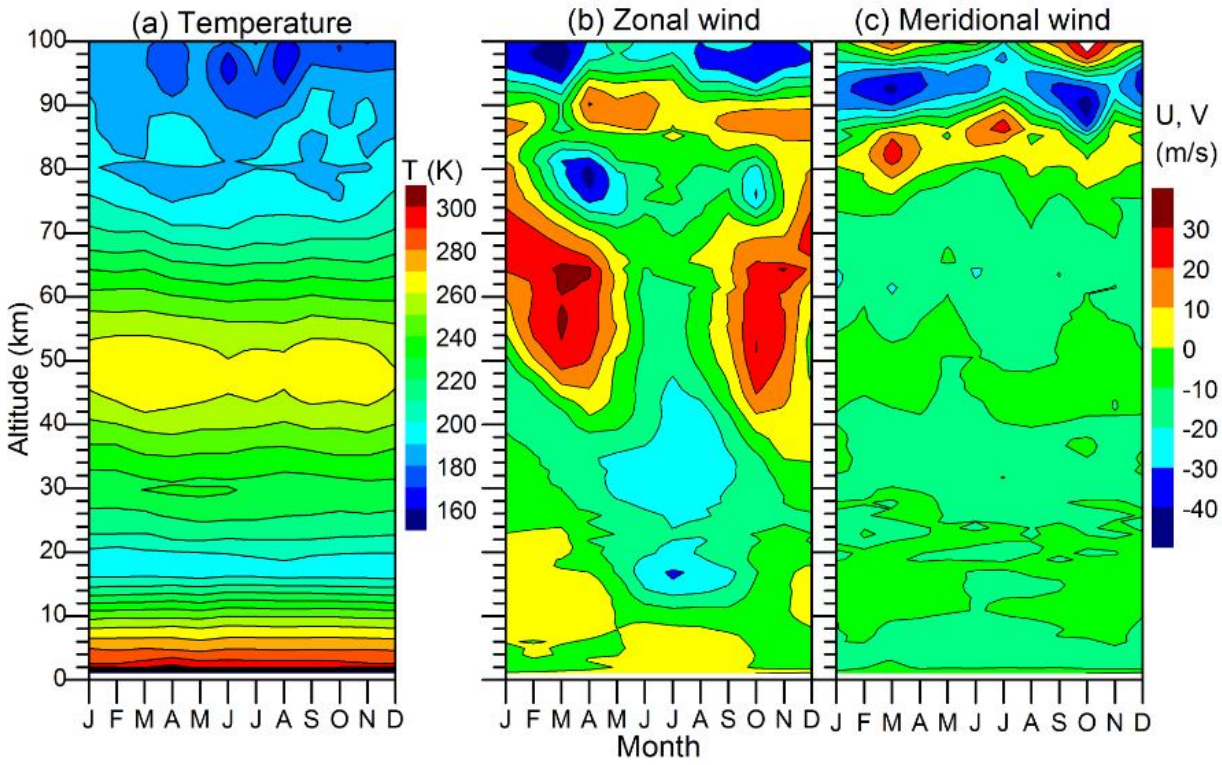

770

771 **Figure 2**. Climatological monthly mean contours of (a) temperature, (b) zonal wind and (c)
772 meridional wind obtained over Gadanki region combining a variety of instruments listed in
773 Table 2.

774

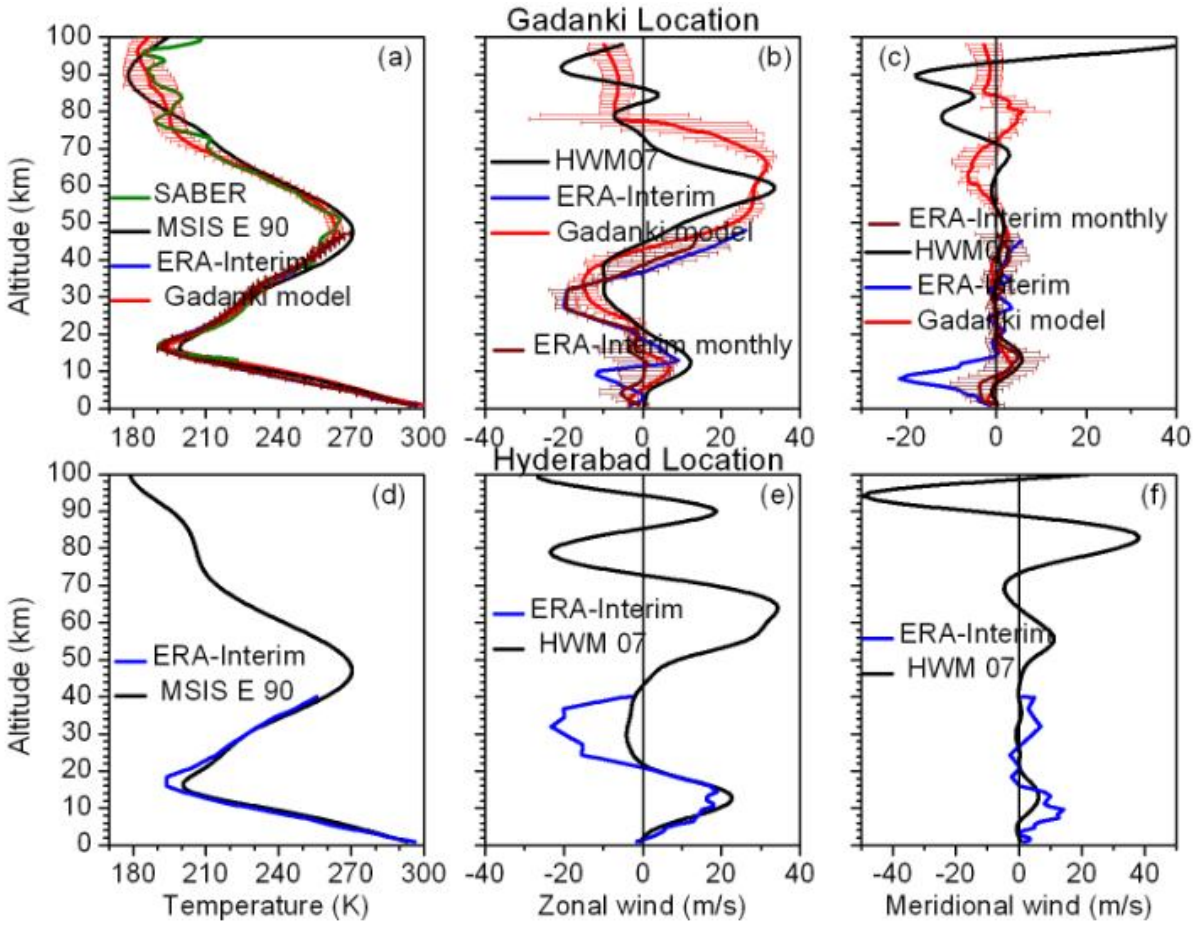

Figure 3. Profiles of (a) temperature (b) zonal wind and (c) meridional wind obtained using ERA-interim data products for 17 March 2012, 12 UTC over Gadanki region. Profiles obtained from variety of sources over Gadanki (Gadanki model) listed in Table 2 are also superimposed in the respective panels for comparison. Plots (d)-(e) are same as (a)-(c) but obtained for Hyderabad on 8 March 2010. Temperature profile obtained from MSISE-90 and zonal and meridional winds obtained from HWM 07 for the same day are also provided in the respective panels.

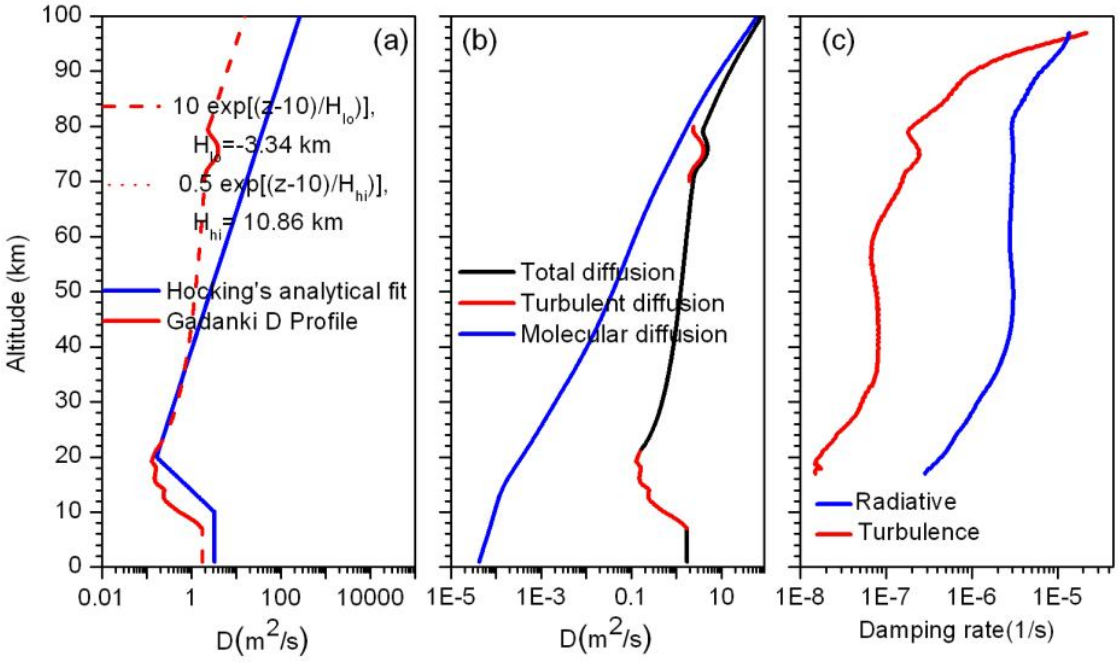

Figure 4. (a) Profile of eddy diffusitvity (thick red line) obtained from Gadanki MST radar (Rao et al., 2001) in the tropopshere, lower stratopshere and mesopshere. Fitted profile (dotted line) with exponetial function is also shown. Hocking's (Hocking 1991) analytical curve (extrapolated) is also superimposed for comparsion. (b) Profiles of eddy, molecualr, and total diffusivity. (c) radiative, and diffusive damping rates.

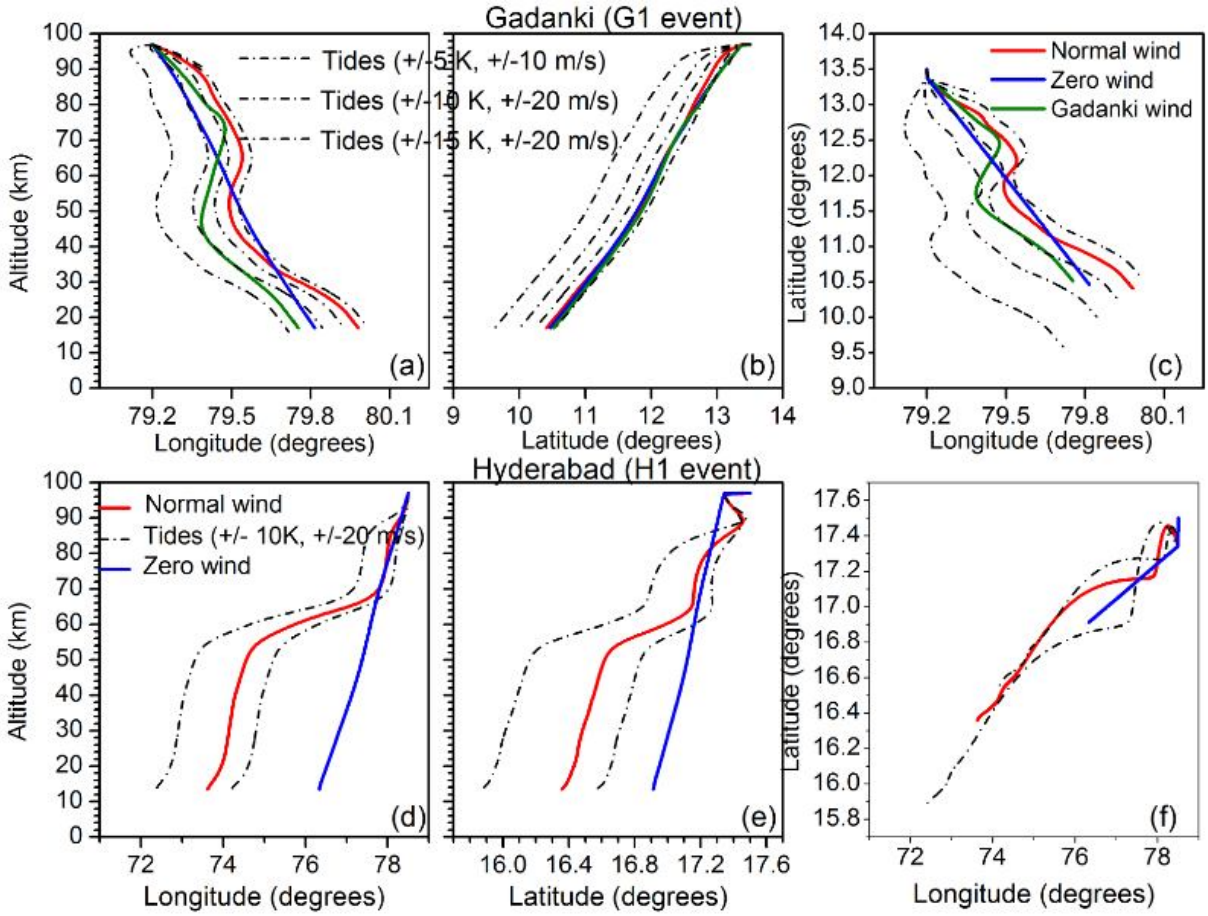

Figure 5. Ray paths for the wave event G1 in the (a) Longitude-Altitude, (b) Latitude-Altitude, and (c) Longitude-Latitude cross sections. Ray paths obtained while considering different background wind conditions (normal wind, zero wind and Gadanki model wind) and the day-to-day variability of tides are also superimposed (dotted lines). (d)-(f) same as (a)-(c) but for the wave event H1. Note that Gadanki atmospheric model wind is not used for the wave events over Hyderabad.

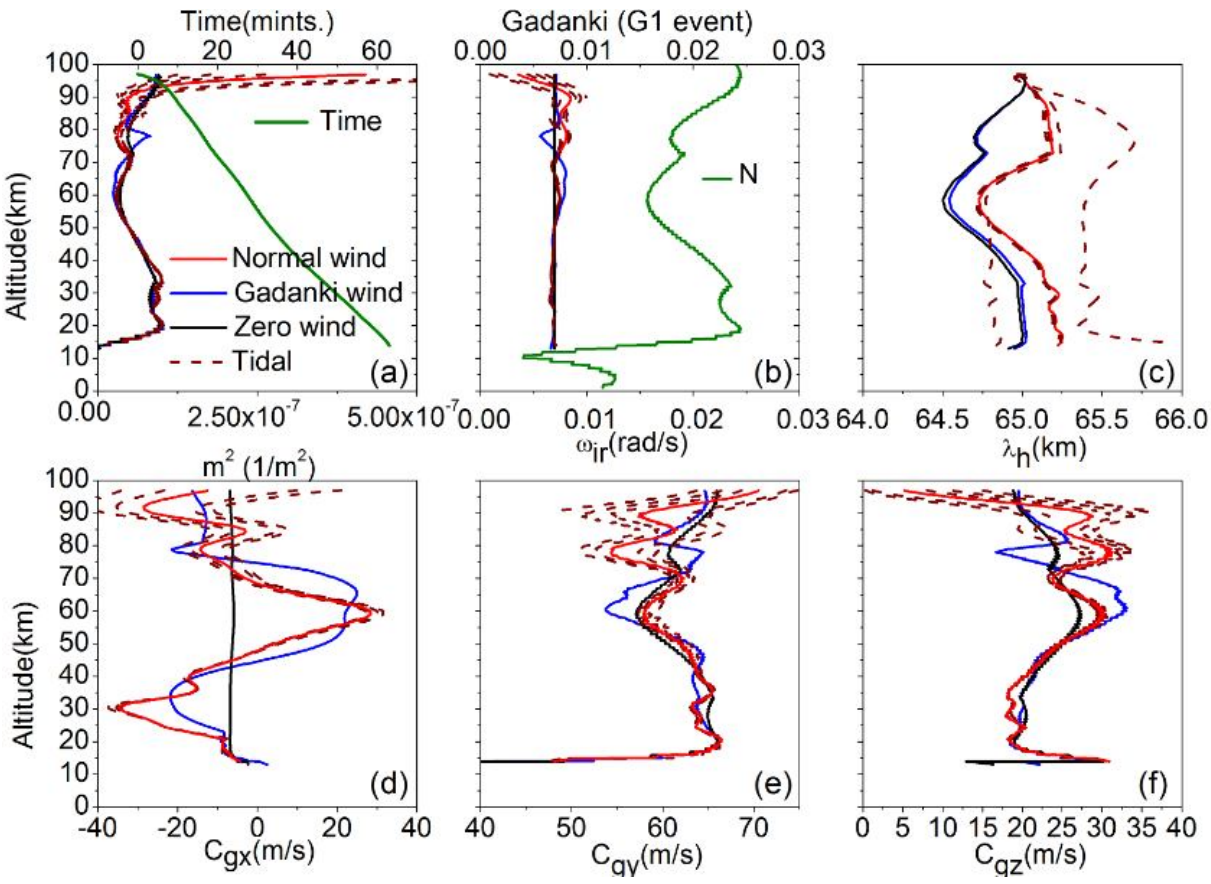

Figure 6. Profiles of (a) square of vertical wave number (m^2), (b) intrinsic frequency (ω_{ir}) and Brunt Väisälä frequency (N) (green), (c) horizontal wavelength (d) zonal, (e) meridional, and (f) vertical group velocities for the wave event G1. Profiles of the same obtained while considering the three different background winds (different colored lines) and the day-to-day variability of tides are also superimposed (dotted lines) in the respective panels. The observation time at the ray-start and according times along the ray time is also shown in (a) with axis on the top.

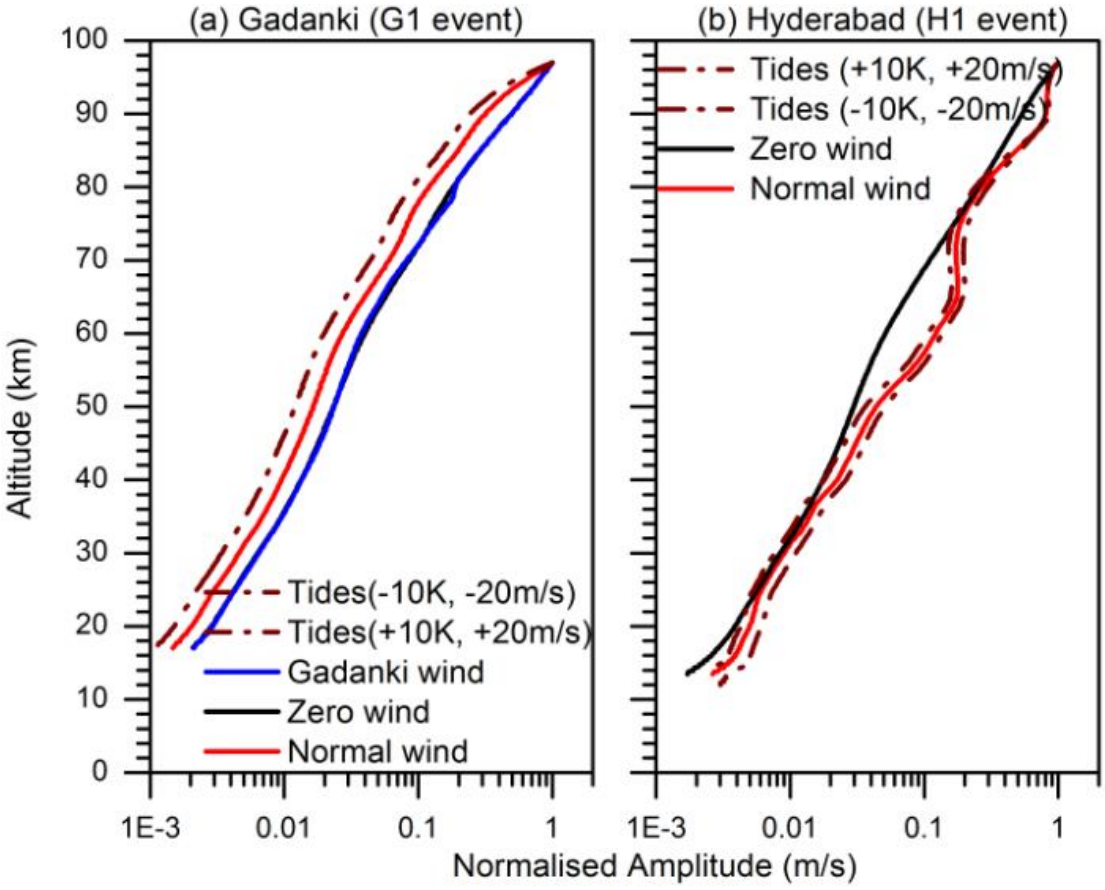

Figure 7. Normalised amplitudes of gravity waves observed for the wave events (a) G1, and (b) H1, over Gadanki and Hyderabad, respectively. Amplitudes with three different background wind conditions along with different tidal amplitudes are also shown.

827

828

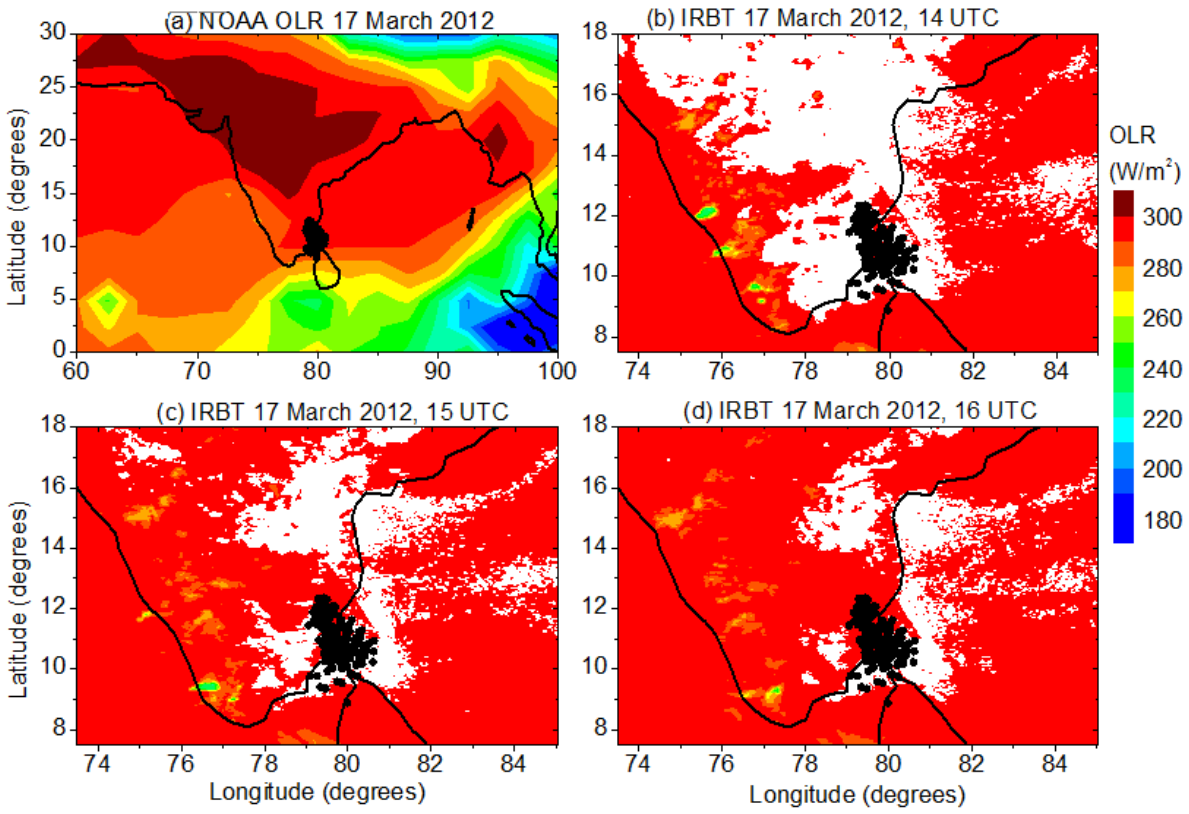

829

830 **Figure 8**. Daily mean latitude-longitude section of (a) OLR observed using NOAA products over
831 Indian region on 17 March 2012. (b)-(d) same as (a) but for IRBT observed at 14 UTC, 15
832 UTC, and 20 UTC, respectively. Open (closed) circles in (a) (b-d) depict the terminal points of
833 the ray paths shown in Figure 4.

834

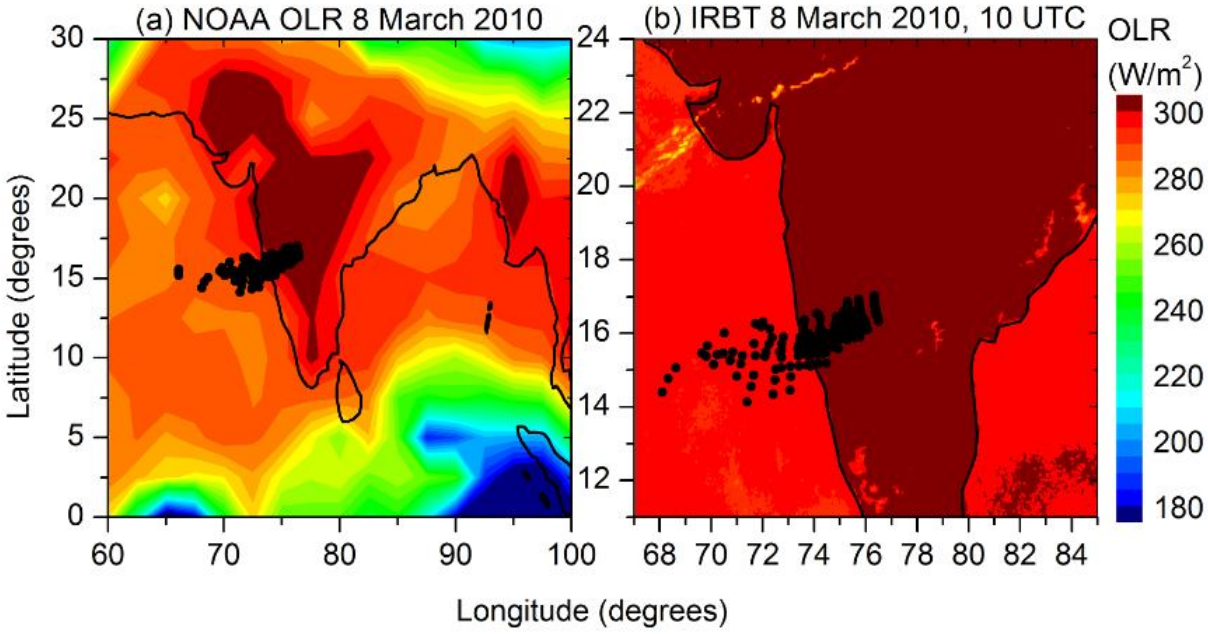

Figure 9. Same as Figure 8 but for wave events observed over Hyderabad on 8 March 2010. Note that IRBT is shown only for 10 UTC.

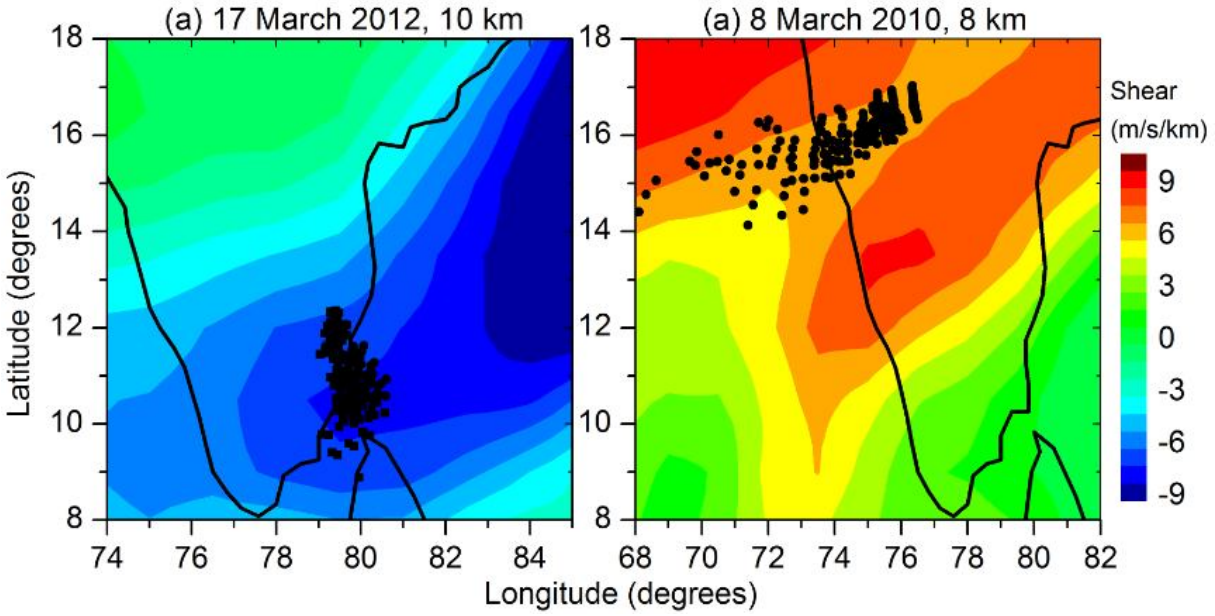

Figure 10. Latitude-longitude section of vertical shear in the horizontal wind observed using ERA-Interim data products on (a) 17 March 2012 at 10 km, (b) 8 March 2010 at 8 km. Filled circles depicts the terminal points of the ray paths estimated using three different wind conditions and tidal amplitudes.

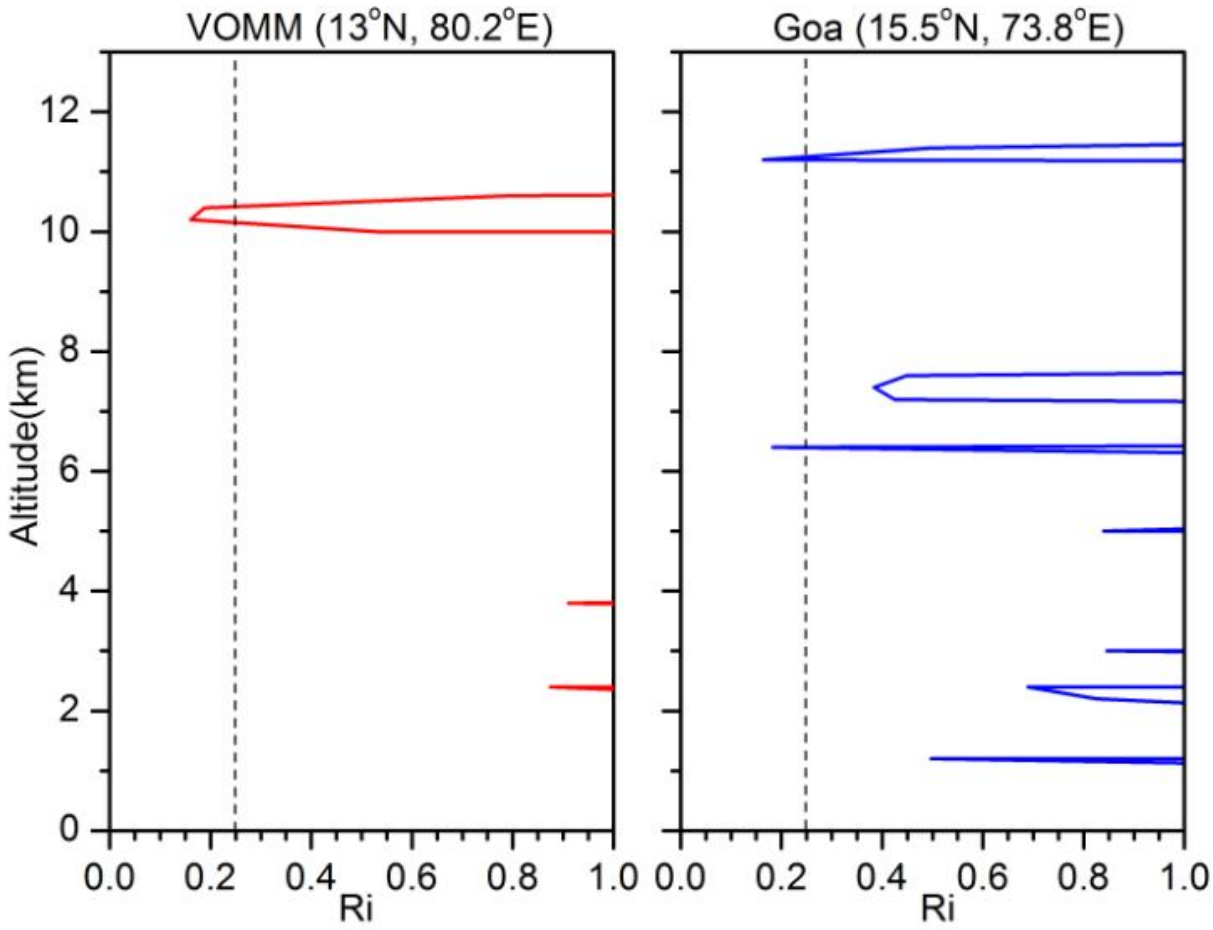

Figure 11. Profiles of Richardson number calculated close to the termination point using radiosonde data for (a) VOMM (Gadanki) and (b) Goa (Hyderabad) locations.